

pubs.acs.org/cm Article

# Local Structure Distortion Induced Broad Band Emission in the All-Inorganic BaScO<sub>2</sub>F:Eu<sup>2+</sup> Perovskite

Shruti Hariyani and Jakoah Brgoch\*



Cite This: Chem. Mater. 2020, 32, 6640-6649



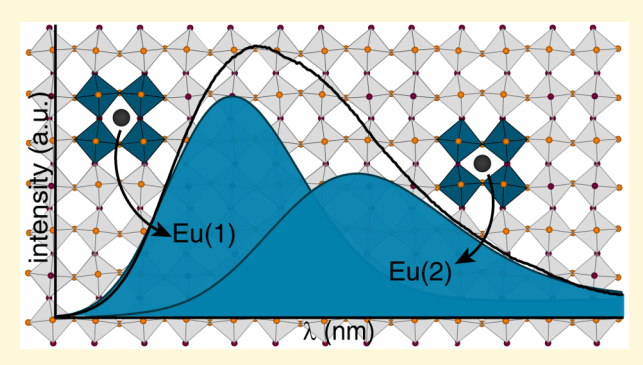
ACCESS

III Metrics & More

Article Recommendations

Supporting Information

ABSTRACT: Perovskites are a class of materials with applications in photovoltaics, solid-state lighting, and catalysis. Extensive research has gone into modifying the chemical composition of these distortion-prone structures to manipulate and achieve their tremendous physical properties. Here, we report a BaScO<sub>2</sub>F perovskite that, when doped with Eu<sup>2+</sup>, produces a highly efficient cyan emission stemming from the structure's high symmetry and dense connectivity. However, the emission peak is broader than expected and steady-state, temperature-dependent, and time-resolved photoluminescence spectroscopy reveals the presence of two distinct emission peaks despite a single rare-earth substitution site. Ab initio calculations subsequently prove that substituting the smaller Eu<sup>2+</sup> induces an unexpected local



structure distortion driven by zone-boundary octahedral tilting. This produces two different local coordination environments around  $Eu^{2+}$  that cause the dual emission. This work shows the critical need to analyze local distortions in phosphors upon rare-earth substitution, especially in perovskites on the verge of structural instabilities.

# 1. INTRODUCTION

Phosphor-converted white light-emitting diodes (pc-LEDs) provide the most accessible pathway to a next-generation light source with longer operating lifetimes, higher luminous efficacy, and environmentally benign components compared to traditional fluorescent and incandescent bulbs. 1,2 Considering the global need to reduce electricity consumption, these devices are becoming the ubiquitous light source for daily life. The most common method to produce white light in these devices is by combining a blue InGaN LED chip ( $\lambda_{\rm em} \approx 450$ nm) with a yellow-emitting phosphor, such as Ce<sup>3+</sup> substituted yttrium aluminum garnet. The rare-earth ion in the host crystal structure partially absorbs the LED's emission and downconverts the photons to longer wavelengths, creating an emission that spans the visible spectrum, thereby appearing as white light. 3,4 This method generates a functional white light but has the drawback of producing a cool, blue-tinted light with poor color rendering  $(R_a < 75)$  and high correlated color temperature (CCT > 4500 K) due to the lack of a red spectral component.<sup>5</sup> Adding in a second, red-emitting phosphor such as K<sub>2</sub>SiF<sub>6</sub>:Mn<sup>4+</sup> or CaAlSiN<sub>3</sub>:Eu<sup>2+</sup> can improve the CRI and CCT, although at increased production cost.<sup>6</sup> Moreover, this approach always lacks photons in the 400-450 nm region, which is vital for creating full-spectrum white light.2

An alternative method to generate white light is by combining red, green, and blue-emitting phosphors excited by a UV-LED ( $\lambda \approx 400$  nm). This approach can also produce warm white light with the added advantage of broad coverage in the blue to near-UV region.<sup>7</sup> Incorporating three phosphors

as the primary visible light source also creates a wider color gamut that allows access to a range of colors for greater color selectivity and tunability. One drawback, however, is that all three phosphors must be highly efficient due to the inherent Stoke's loss from the down-conversion process. Additionally, the phosphors must possess a narrow emission with a minimal full width at half-maximum (fwhm) to limit spectral overlap between the various excitation and emission spectra of each phosphor. As a result, the search for new blue, green, and redemitting phosphors is centered on identifying materials with a highly efficient, extremely narrow emission.

Current investigations in the development of efficient and narrow-emitting phosphors have illuminated certain design rules to increase the probability of discovering these materials. One of the initially proposed criteria for developing narrow-emitting phosphors is to identify compounds with a single crystallographic site of appropriate size and valency for rare-earth, i.e.,  $Ce^{3+}$  or  $Eu^{2+}$ , substitution. Examples of single-site, narrow-emitting materials include  $Sr[Be_6ON_4]:Eu^{2+}$  (fwhm = 35 nm, 1400 cm<sup>-1</sup>), RbNa<sub>3</sub>(Li<sub>3</sub>SiO<sub>4</sub>)<sub>4</sub>:Eu<sup>2+</sup> (fwhm = 22.4 nm, 980 cm<sup>-1</sup>), and

Received: May 15, 2020 Revised: July 7, 2020 Published: July 8, 2020





 $BaLi_2[Be_4O_6]{:}Eu^{2+}$  (fwhm = 25 nm, 1200 cm  $^{-1}),^2$  among others.  $^{12,13}$  Remarkably, there are cases where multiple substitution sites also yield a narrow emission. The narrow red emission in  $Sr[LiAl_3N_4]:Eu^{2+}$  (fwhm = 50 nm, 1180 cm<sup>-1</sup>) is attributed to the highly symmetric cuboid-like environment surrounding the two crystallographically independent Sr atoms in the structure. 14 This conclusion has shifted the design consideration primarily toward crystal structures containing cuboid coordination environments, even if multiple crystallography sites are present. This is corroborated by the Ba<sub>3</sub>Y<sub>2</sub>B<sub>6</sub>O<sub>15</sub>:Ce<sup>3+</sup> phosphor, which has a fwhm of only 70 nm (3362 cm<sup>-1</sup>) despite the presence of two Y sites for Ce<sup>3+</sup> substitution. The nearly identical [YO<sub>6</sub>] environments allow for uniform crystal field splitting of the Ce<sup>3+</sup> 5d orbitals, giving rise to narrow emission. 15 On the contrary, the single Ba site in Ba<sub>2</sub>Mg(BO<sub>3</sub>)<sub>3</sub>:Eu<sup>2+</sup> is highly anisotropic with three long and six short Ba-O bonds in the [BaO<sub>9</sub>] polyhedra, but severe distortion occurs upon Eu2+ substitution leading to broad orange emission (fwhm = 92 nm). 16 Therefore, understanding the propensity for local structural distortions around the rareearth is also essential when developing new phosphors.

The prerequisites for narrow emission also increase the probability of highly efficient emission. All of the aforementioned phosphors contain symmetric polyhedra that serve as the basis for the narrow emission. They also tend to produce rigid, dense bonding networks. The extensive connectivity inhibits access to soft phonon modes, which are pathways for nonradiative relaxation. This results in the increased likelihood for a material to possess an (internal) photoluminescent quantum yield (PLQY) near unity. The Debye temperature  $(\Theta_{\rm D})$  has recently been used as a proxy of structural rigidity and has been used to screen crystal structure databases for host structures with predicted high efficiency. This methodology was vital in the discovery of the NaBaB<sub>9</sub>O<sub>15</sub>:Eu<sup>2+</sup> phosphor  $(\Theta_D = 729 \text{ K})$  which possesses a highly efficient (PLQY = 95%) and narrow emission (fwhm = 34.5 nm,  $1849.5 \text{ cm}^{-1}$ ). 17 There is no doubt that structures with a rigid and dense framework are instrumental in the development of nextgeneration luminescent materials.

One structure type that meets all of the proposed criteria but has not been extensively explored as phosphor hosts are perovskites. Perovskites are potentially ideal due to the single, highly symmetric cuboctahedrally coordinated A-site cation that sits in the octahedral cavity created by  $[BX_6]$  octahedron. Perovskites can also possess very high Debye temperatures (>400 K). The biggest limitation of these compounds is that a majority of perovskites are semiconductors. The narrow bandgap (<3.3 eV) increases the probability of emission occurring in the UV and quenching via photoionization. 19 Additionally, many perovskites contain transition metals meaning there is no suitable site for rare-earth substitution. There have been some insulating  $ABX_3$  systems studied as phosphors, such as  $BaHfO_3:Eu^{2+}$  and  $MTiO_3:Eu^{2+}$  (M = Ca, Sr, Ba), although these systems have not been investigated in depth since the excitation maximum tends to fall in the UV-C region ( $\lambda_{\rm ex} = 250{-}260$  nm). <sup>20,21</sup>

These hurdles have motivated researchers to study double perovskites ( $A_2BB'X_6$ ) and vacancy ordered double perovskites ( $A_2BX_6$ ) as phosphor hosts. These perovskites perform the down-conversion process as desired; however, these structures contain multiple substitution sites or are only able to incorporate line-emitters such as Eu<sup>3+</sup> or luminescent transition metals such as Bi<sup>3+</sup> or Sb<sup>3+</sup>, limiting their

application. <sup>24,25</sup> One remaining avenue of the perovskite system to explore is mixed anionic perovskites, with general formula  $ABO_2F$ . There are only a few  $A^{2+}B^{3+}O_2F$  compositions previously reported that are suitable for rare-earth substitution, including BaScO<sub>2</sub>F, BaFeO<sub>2</sub>F, and BaInO<sub>2</sub>F. Not surprisingly, BaFeO<sub>2</sub>F and BaInO<sub>2</sub>F do not possess a wide bandgap to be a viable phosphor host. <sup>26,27</sup> However, beyond a preliminary report, BaScO<sub>2</sub>F has not been widely investigated as a phosphor. <sup>28</sup> This warrants further investigation into the electronic structure of this compound to determine its capability as a potential phosphor host for highly efficient, narrow emission.

In this work, we first use ab initio band structure calculations to confirm the wide bandgap of cubic BaScO<sub>2</sub>F followed by the synthesis of the BaScO<sub>2</sub>F:Eu<sup>2+</sup> phosphor using high-temperature sintering. The average cubic structure was confirmed through Rietveld refinement. Substituting Eu<sup>2+</sup> in the perovskite produced bright cyan luminescence with a high quantum yield; however, the emission peak was unexpectedly broad and corresponded to two Eu<sup>2+</sup> luminescent sites. Indeed, steadystate, temperature-dependent, and time-dependent photoluminescent measurements all suggest the presence of two distinct emission peaks despite the presence of a single substitution site in the cubic perovskite structure. We, therefore, turned to ab initio calculations to reveal that the incorporation of Eu<sup>2+</sup> in the perovskite crystal structure causes a zone-boundary instability leading to octahedral tilting. The loss of symmetry gives rise to two distinct local Eu<sup>2+</sup> coordination environments. The subtle differences in the resulting europium polyhedral volume and crystal field splitting ultimately cause the observed two different emissions.

#### 2. METHODOLOGY

**2.1. Experimental Procedure.** Polycrystalline samples of  $BaScO_2F$  and  $Ba_{1-x}Eu_xScO_2F$  ( $x=0.01,\ 0.02,\ 0.03,\ and\ 0.04$ ) were prepared by combining  $BaCO_3$  (Johnson Mathey, 99.99%),  $Sc_2O_3$  (Alfa Aesar 99.99%),  $BaF_2$  (Sigma-Aldrich, 99.99%), and  $Eu_2O_3$  (Alfa Aesar, 99.99%) in the appropriate stoichiometric ratios. The mixtures were ground with an agate mortar and pestle in an acetone medium before milling with a high-energy ball mill (Spex 8000 M Mixer/Mill) for 100 min. The resulting homogeneous powder was pressed into a 6 mm pellet and placed in an alumina crucible (AdValue Technology) on top of a bed of sacrificial  $BaScO_2F$  powder to avoid reaction with the vessel. This crucible was placed between two crucibles containing activated carbon (Sigma-Aldrich) and Ti powder (Sigma-Aldrich, 99.5%) to obtain a highly reducing atmosphere. The pellets were fired in a tube furnace at 1200 °C for 8 h under flowing 15%  $H_2/85\%$   $N_2$  gas with a heating and cooling rate of 3 °C per minute.

The products were reground in an agate mortar and pestle. Preliminary powder X-ray diffraction (X'Pert3 PANalytical; Cu  $K\alpha$ ,  $\lambda$  = 1.541 83 Å) revealed a slight BaF<sub>2</sub> impurity, which was removed by dispersing the powder in hot deionized water and centrifuging (Dynac centrifuge) for 30 min. The water was decanted, and the powder was dried by mixing with acetone and heating at 100 °C. Final phase purity was confirmed through high-resolution synchrotron X-ray powder diffraction using the 11-BM at the Advanced Photon Source (APS) at Argonne National Laboratory. The data were collected at 100 K with a calibrated wavelength of 0.457 861 Å. Rietveld refinements were performed using the EXPGUI interface of GSAS.<sup>29</sup> The background was fit using a shifted Chebyshev function and the peak shaped modeled using a pseudo-Voigt function. The resulting crystal structure was visualized using VESTA.<sup>30</sup>

Optical characterization was completed by mixing the polycrystalline samples with an optically transparent resin (GE Silicones, RTV615) and depositing on a quartz slide (Chemglass). Photoluminescent spectra were obtained using a PTI fluorescence

spectrophotometer with a 75 W xenon arc lamp for excitation. The internal photoluminescent quantum yield (PLQY) was determined using the method of de Mello et al. employing a Spectralon coated integrating sphere (150 mm diameter, Labsphere) with a 340 nm excitation. Luminescent measurements at 10 K were done using a SHI-APD model DE-204N cryostat with a Sumitomo HC-4E 1 helium compressor from Cryo Industries of America, Inc. with a 351 nm excitation source and Triax 550 (Horiba Jobin-Yvon) spectrometer. The photoluminescent lifetime was measured using a Horiba DeltaFlex Lifetime System with a NanoLED N-330 nm LED. A Janis cryostat (VPF-100) was employed for all temperature-dependent measurements from 80 to 500 K.

**2.2. Computational Procedure.** The Vienna ab initio simulation package (VASP) was used for the density functional theory (DFT) calculations. <sup>32</sup> All calculations employed a plane-wave basis set with projector-augment-wave (PAW) pseudopotentials. <sup>33</sup> The exchange and correlation were described by the Perdew–Burke–Ernzerhof (PBE) functional. <sup>34</sup> The Debye temperature was calculated using the quasi-harmonic Debye model, which has been shown to be an accurate approximation. <sup>35</sup> Following eq 1,  $\Theta_{\rm D}$  is determined from the spherical average of the sound velocity where  $k_{\rm B}$  and  $\hbar$  are the Boltzmann constant and Planck's constant, respectively, M is the molar mass, N is the number of atoms, V is the volume of the unit cell, and  $f(\sigma)$  is the value obtained using eq 2 where  $\sigma$  is the Poisson ratio. The elastic moduli, including the bulk modulus ( $B_{\rm H}$ ) and  $\nu$  were calculated using the Voigt–Reuss–Hill (VRH) approximations based on the elastic constants ( $C_{ij}$ ) following the method of Wu et al. <sup>36</sup>

$$\Theta_{\rm D} = \frac{\hbar}{k_{\rm B}} [6\pi^2 V^{1/2} n_a]^{1/3} \sqrt{\frac{B_{\rm H}}{M}} f(\sigma)$$
 (1)

$$f(\sigma) = \left\{ 3 \left[ 2 \left( \frac{2}{3} \frac{1+\nu}{1-2\nu} \right)^{3/2} + \left( \frac{1}{3} \frac{1+\nu}{1-2\nu} \right)^{3/2} \right]^{-1} \right\}^{1/3}$$
 (2)

To account for the statistical site-sharing between O and F, a 2  $\times$  2  $\times$ 2 unit cell with all possible distributions of O and F atoms was enumerated using the "Supercell" software.<sup>37</sup> Static energy calculations were performed on the 2664 optimized models. The lowest total energy ordering was selected for further computational analysis. To determine the effect of Eu<sup>2+</sup> substitution on the overall structure of BaScO<sub>2</sub>F, the lowest energy  $2 \times 2 \times 2$  supercell (40 atoms) and a 2  $\times$  2  $\times$  4 supercell (80 atoms) model was constructed where one or two Ba2+ atom(s) were substituted by Eu2+. All structural optimizations implemented an electronic convergence criterion set to  $1 \times 10^{-8}$  eV and an ionic convergence criterion set to  $1 \times 10^{-6}$  eV/ Å. An energy cutoff of 500 eV was used, and the integration of the first Brillouin zone was carried out using a Monkhorst-Pack k-point grid of  $\approx 1000 \text{ k-points/atom.}^{38}$  The rare-earth substituted systems required using the PBE+U method to describe the highly correlated 4f electrons, where U = 7.62 for Eu<sup>2+</sup>.<sup>39</sup> Finally, phonon dispersion curves were calculated using the PHONOPY package, which uses the modified Parlinski-Li-Kawazoe ab initio force constant method. 40 To model the anharmonic potential energy surfaces of BaScO<sub>2</sub>F and EuScO<sub>2</sub>F attributed to imaginary phonons, ModeMap, an opensource package, was used. 41 The calculations involve constructing a series of structures that incrementally distort the  $[BX_6]$  octahedra along the imaginary phonon eigenmode across a range of amplitudes of the normal-mode coordinate Q and determining the static total energy.4

# 3. RESULTS AND DISCUSSION

**3.1. Electronic Structure, Synthesis, and Crystallog-raphy.** Perovskites are widely known for applications in solar cells, transistors, and many other semiconducting applications. However, as a phosphor, the host crystal structure must have a sufficiently wide bandgap (>3.3 eV) to allow the electronic transitions on the rare-earth luminescent center to occur unencumbered. If the bandgap is too small, the

phosphor's luminescence can be quenched via photoionization. The electronic band structure of BaScO<sub>2</sub>F was calculated using the PBE functional and revealed an (underestimated) indirect bandgap value of 3.05 eV (Figure S1). This bandgap is larger than the isostructural BaBOF<sub>2</sub> (B = Fe and In) perovskites but, more importantly, is wide enough to accommodate the 4f  $\leftrightarrow$  5d transitions of a rare-earth ion. Although the bandgap is slightly smaller than 3.3 eV, quenching from photoionization may occur. Decomposing the total electronic density of states into the partial density of states, as seen in Figure 1a, depicts the O 2p states sitting at

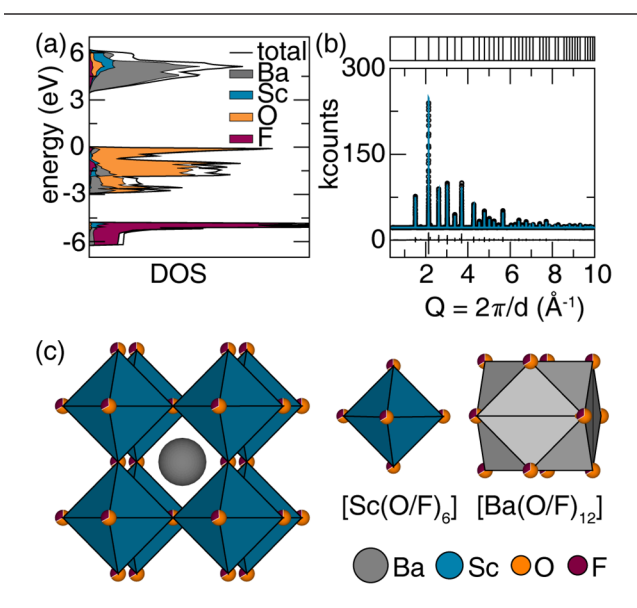


**Figure 1.** (a) Density of states of BaScO<sub>2</sub>F calculated using the PBE functional. (b) Rietveld refinement of high-resolution synchrotron X-ray diffraction of  $Ba_{0.96}Eu_{0.04}ScO_2F$ . The measured data are represented by black circles, the refinement fit is in blue, and the black line represents the difference. (c) Structure of  $BaScO_2F$  composed of  $[Sc(O/F)_6]$  and  $[Ba(O/F)_{12}]$  polyhedra.

the top of the valence band, with the F 2p states sitting directly beneath. The bottom of the conduction band is dominated by the Sc 3d states with some contribution from the Ba 5d states, which hybridize with the O and F 2p states. The Debye temperature was determined to be 517 K, which suggests this phosphor should show relatively efficient emission upon rareearth substitution. These electronic structure calculations support that  $BaScO_2F$  is a rigid, covalent system with a wide bandgap, making it a promising phosphor host.

BaScO<sub>2</sub>F has been previously synthesized by reacting BaF<sub>2</sub> and Sc<sub>2</sub>O<sub>3</sub> at 1000 °C for 72 h with several intermittent grindings. Following this synthetic procedure here resulted in a poorly crystalline product with major impurities corresponding to starting materials. This phase has also been reported from sintering BaCO<sub>3</sub>, BaF<sub>2</sub> Sc<sub>2</sub>O<sub>3</sub>, and EuF<sub>3</sub> at 1100 °C. However, the product obtained following this route showed substantial BaF<sub>2</sub> impurities. The title phase could finally be obtained as a nearly phase pure product by mixing BaCO<sub>3</sub>, BaF<sub>2</sub> Sc<sub>2</sub>O<sub>3</sub>, and Eu<sub>2</sub>O<sub>3</sub> in the appropriate stoichiometric ratios and reacting at 1200 °C for 8 h. The body color of the obtained powder was beige. Powder X-ray diffractograms showed the product crystallized in the cubic space group  $Pm\overline{3}m$  with minor BaF<sub>2</sub> impurities (Figure S2a). BaF<sub>2</sub> is slightly soluble in water and can be washed to remove the impurity; <sup>46</sup> however, many oxyfluorides are also unstable with

respect to moisture.  $^{47,48}$  Fortunately, the only physical effect of washing  $Ba_{1-x}Eu_xScO_2F$  (x=0,0.01,0.02,0.03,0.04) in hot deionized water was that the body color of the powder became white. The resulting powders showed no degradation after washing and were confirmed phase pure using laboratory powder X-ray diffraction (Figure S2b). The inclusion of  $Eu^{2+}$  in the structure was confirmed through a decrease in the lattice parameters, following Vegard's law (Figure S3). The plateau of the lattice parameters with increasing  $Eu^{2+}$  substitution indicates that a substitution limit has potentially been reached.

The average cubic structure of  $BaScO_2F$  and  $Ba_{0.96}Eu_{0.04}ScO_2F$  was analyzed using Rietveld refinements of high-resolution synchrotron powder X-ray diffraction plotted in Figures S4 and 1b, respectively. The refinement statistics for  $BaScO_2F$  and  $Ba_{0.96}Eu_{0.04}ScO_2F$  are provided in Table 1, and

Table 1. Rietveld Refinement Data and Statistics for  $BaScO_2F$  and  $Ba_{0.96}Eu_{0.04}ScO_2F$ 

	refined formula	
	BaScO <sub>2</sub> F	$Ba_{0.96}Eu_{0.04}ScO_2F$
radiation type, $\lambda$ (Å)	synchrotron, 0.457861	
2 heta range (deg)	0.5-50	
temperature (K)	100	
crystal system	cubic	
space group; Z	$Pm\overline{3}m; 1$	
lattice parameters (Å)	4.17036(2)	4.15754(1)
volume (ų)	72.531(1)	71.864(1)
$R_{\rm p}$	0.0664	0.1099
$R_{ m wp}$	0.1017	0.1565
$X^{2}$	8.685	16.69

the refined crystal structure data are provided in Table S1 and Table S2, respectively. The refinements show excellent agreement with the published crystal structure employed as the initial model and corroborate the average cubic  $Pm\overline{3}m$  structure. The formation of the cubic perovskite structure is also in agreement with the Goldschmidt tolerance factor, provided in eq 3 where  $r_A$ ,  $r_B$ ,  $r_O$ , and  $r_F$  are the atomic radii of the A and B cations and O and F, respectively. The calculated value of t for BaScO<sub>2</sub>F is 0.997, corresponding to a cubic structure (0.9 < t < 1.0).

$$t = \frac{r_A + 0.66r_O + 0.33r_F}{\sqrt{2} \left( r_B + 0.66r_O + 0.33r_F \right)}$$
(3)

BaScO<sub>2</sub>F was the first cubic perovskite reported with the  $A^{2+}B^{3+}$  [X<sup>2-</sup>]<sub>2</sub>[Y<sup>-</sup>] stoichiometry.<sup>28</sup> The crystal structure, depicted in Figure 1b, corresponds to a traditional ABO<sub>2</sub>F perovskite crystallizing in the space group  $Pm\overline{3}m$  (no. 221). The unit cell is composed of corner connected  $[Sc(O/F)_6]$ with the A-site cation sitting comfortably in the octahedral cavity with cuboctahedral [Ba(O/F)<sub>12</sub>] coordination. The anion site is filled with disordered fluorine and oxygen in an approximate 33%:67% ratio, which was confirmed by <sup>19</sup>F NMR.<sup>28</sup> As a result, in the refinements performed here this ratio was kept constant, considering it is not possible to distinguish between O and F with X-ray diffraction.<sup>51</sup> The resulting refined  $Sc(O/F)_6$  octahedra in the host are composed of six equal Sc-O/F bonds, 2.0852 Å in length, while the Ba cuboctahedron has a polyhedral volume of 60.44 Å<sup>3</sup> and is composed of Ba-O/F bonds 2.95 Å in length. Considering the atomic radii of the cations, the single  $Ba^{2+}$  site ( $r_{12\text{-coord}} = 1.61$ 

Å) is the only site for Eu<sup>2+</sup> substitution ( $r_{12\text{-coord}} = 1.48$  Å;  $r_{6\text{-coord}} = 1.17$  Å) because the Sc<sup>3+</sup> site is too small ( $r_{6\text{-coord}} = 0.745$  Å). Eu<sup>2+</sup> substitution on the Ba<sup>2+</sup> site was verified by analyzing the refined lattice parameters and *A*-site polyhedral volume; the lattice parameters show a minor (0.31%) decrease with the average Ba polyhedral volume decreasing by 0.94% to 59.87 Å<sup>3</sup>.

**3.2. Photoluminescence Properties.** Eu<sup>2+</sup> was substituted for Ba<sup>2+</sup> into the structure following Ba<sub>1-x</sub>Eu<sub>x</sub>ScO<sub>2</sub>F (x = 0.01, 0.02, 0.03, 0.04). Measuring the photoluminescent excitation spectrum reveals a broad excitation from 250–450 nm. (Figure 2a) The excitation band has three distinct maxima

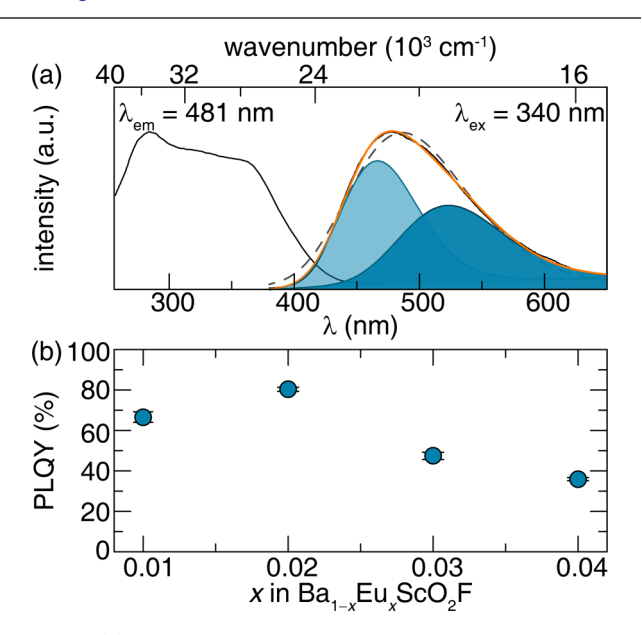


**Figure 2.** (a) Room temperature excitation and emission spectra of  $Ba_{0.98}Eu_{0.02}ScO_2F$ . The emission data cannot be fit to one Gaussian function (dashed gray line) but can be well described by two Gaussian functions (orange line). (b) Room temperature photoluminescent quantum yield measurements upon 340 nm excitation. The maximum quantum yield of 80.3(5)% is achieved upon 2% Eu substitution.

located at approximately 282, 340, and 365 nm. This broad excitation band allows  $BaScO_2F:Eu^{2+}$  to be excited by UV-B, UV-A, and blue light, making it an extremely versatile phosphor.

Monitoring the emission upon excitation at each of these maxima reveals an identical very bright, cyan emission with a maximum located at 481 nm. The room temperature photoluminescent quantum yield (PLQY) of  $Ba_{1-x}Eu_xScO_2F$  ( $x=0.01,\,0.02,\,0.03,\,0.04$ ) showed that an exceptional PLQY of 80.3(5)% could be achieved when x=0.02 using a  $\lambda_{ex}=340$  nm. Increasing the  $Eu^{2+}$  content up to x=0.04 causes the efficiency to decrease by almost half to 35.9(3)%, as shown in Figure 2b. Interestingly, washing the products did not affect the emission spectrum or PLQY of  $Ba_{0.98}Eu_{0.02}ScO_2F$  (Figure S5). The maximum value of the PLQY is competitive with nearly all other cyan-emitting materials like  $Ca_3(PO_4)_2$ : $Eu^{2+}$  (PLQY = 60%) and NaMgBO<sub>3</sub>: $Ce^{3+}$  (PLQY = 93%).  $Ce^{3+}$  The high PLQY undoubtedly stems from the rigid [Sc(O/F)<sub>6</sub>] octahedral network ( $\Theta_D = 517$  K).

Analyzing the emission peak further shows that it covers the blue and cyan regions of the visible spectrum due to its broad full width at half-maximum of 4135 cm<sup>-1</sup> (103 nm) making it possible to produce full-spectrum white light. <sup>54</sup> Indeed, a

highly efficient cyan emission is desirable to fill the "cyan gap" that stems from the incorporation of extremely narrow blueemitting phosphors in lighting devices. 55 However, the experimentally measured broad emission contradicts the initial hypothesis of a narrow emission from a highly symmetric, single substitution site. 11 To better understand the broad emission, the emission curve was first fit to a single Gaussian. This fit, shown as the dashed gray line in Figure 2a, is poor. The shape of a single Gaussian peak, which is commonly used to approximate the rare-earth emission, cannot describe these data. The measured emission peak could only be reasonably fit by deconvoluting the emission into two distinct Gaussian peaks shown in Figure 2a by the orange line. These two Gaussian peaks are separated by ~2335 cm<sup>-1</sup> with the integrated peak areas in an approximate 1:1 ratio. Measuring the emission at 13 K (Figure S6) indicates that the longer wavelength emission peak becomes more prominent compared to the shorter wavelength peak but with significant overlap between the two emission peaks.

The presence of two overlapping peaks even at 13 K suggests the Eu<sup>2+</sup> coordination environments are nearly identical but may still be from distinct luminescent centers. Blasse and co-workers observed a similar phenomenon in Eu<sup>2+</sup> substituted structures containing chains of alkaline earth ions. 56 They observed one main peak and a shoulder in their data that was attributed to the local coordination environment of the activator ion. When a divalent europium ion experiences a combination of negative and positive charges from the nearest-neighbor anion and cation, these charges can cause the Eu<sup>2+</sup> 5d orbitals to orient preferentially, resulting in emission at longer wavelengths from a single crystallographic site.5 However, it was later proven using time-resolved photoluminescent spectroscopy that only a single luminescent lifetime could be obtained for their compounds with a single substitution site, regardless of the presence of the fact that the data showed an emission peak and a shoulder. 58 Therefore, to unequivocally determine if the two peaks in BaScO<sub>2</sub>F:Eu<sup>2+</sup> are arising from the presence of a second independent Eu<sup>2+</sup> site or preferential d-orbital orientation, room temperature photoluminescent lifetime measurements were conducted. The photoluminescent decay of BaScO<sub>2</sub>F:Eu<sup>2+</sup> was monitored using  $\lambda_{\rm ex}$  = 330 nm excitation. The data were fit according to a mono- and biexponential function following eq 4 to determine the origin of the shoulder emission where I is intensity,  $I_0$ ,  $A_1$ , and  $A_2$  are pre-exponential constants,  $\tau_1$  and  $\tau_2$ are decay times for exponential components in microseconds, and t is the measured time.

$$I = I_0 + A_1 e^{-t/\tau_1} + A_2 e^{-t/\tau_2}$$
(4)

According to Figure 3a, it is clear that two distinct emissions contribute to the luminescent lifetime. The biexponential curve (orange line) captures the full decay curve, whereas a monoexponential fit (dashed black line) is not representative of the collected data. The lifetimes are 0.786 and 0.256  $\mu$ s, which are typical of Eu<sup>2+</sup> emission from crystallographically independent substitution sites. Temperature-dependent time-resolved photoluminescent data were also collected from 80 to 480 K to support the observation of dual Eu<sup>2+</sup> emission further. The data could only be adequately fit by two lifetimes at all temperatures, with the lifetimes becoming progressively faster with increasing temperature, as expected (Figure 3b). Most importantly, fitting the linear decay from 320 to 500 K results in two separate decay rates of 0.0031  $\mu$ s/

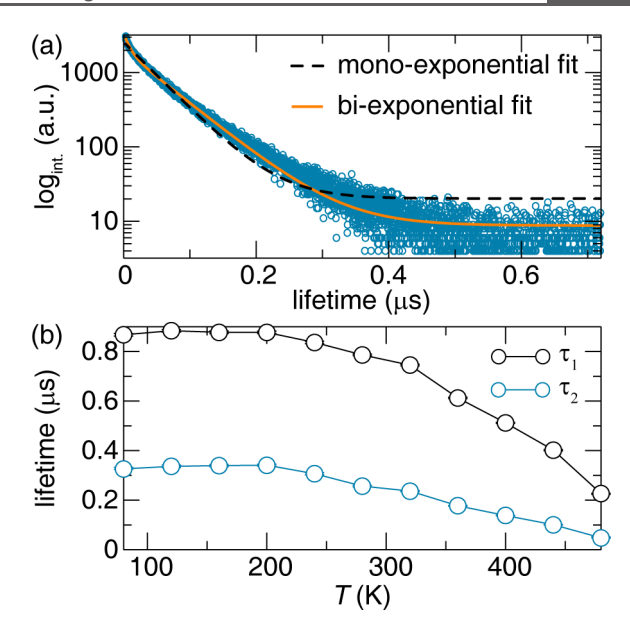


Figure 3. (a) Room temperature photoluminescent lifetime decay curve of  $Ba_{0.98}Eu_{0.02}ScO_2F$ . The dashed black line represents a single exponential fit, while the correct fit is modeled by a biexponential, represented by the orange line. (b) Temperature-dependent photoluminescent lifetime. The rates of decay differ as a function of temperature, signifying two independent emission sources.

K and 0.0011  $\mu s/K$ , further confirming the presence of two separate emissions.

Additional temperature-dependent photoluminescent spectroscopic analysis was carried out to gain further insight into the two emissions in  $BaScO_2F:Eu^{2+}.$  Temperature-dependent photoluminescent emission spectra of  $Ba_{0.98}Eu_{0.02}ScO_2F$  were collected from 80 to 500 K to determine the quenching behavior of the two emissions at elevated temperatures. As seen in Figure 4a, the relative emission intensity remained

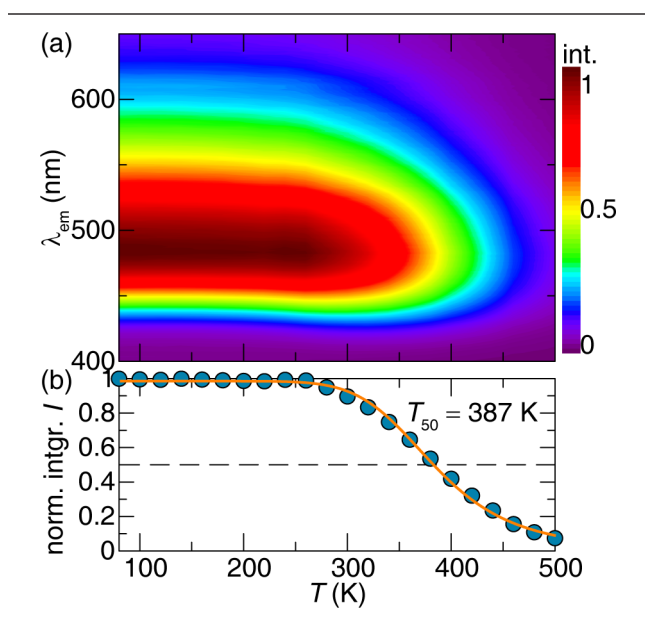


Figure 4. (a) Contour plot of the normalized emission spectra of  $Ba_{0.98}Eu_{0.02}ScO_2F$  excited as 340 nm. (b) Normalized, integrated intensity of the emission peak as a function of temperature. The orange line depicts the fit of the Arrhenius equation, where the activation energy was calculated to be 0.32 eV.

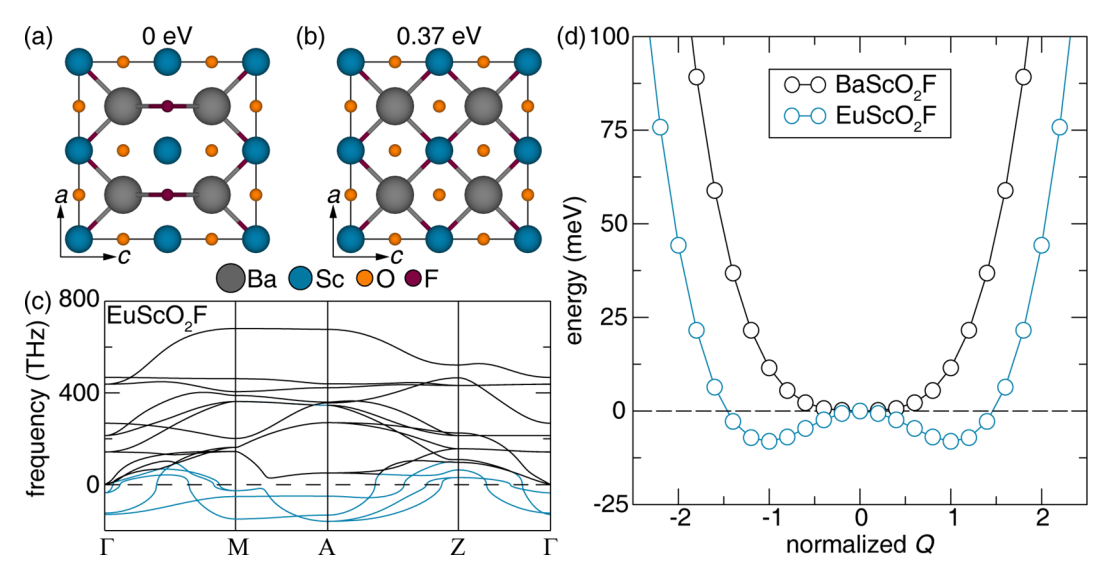


Figure 5. (a) The lowest energy  $2 \times 2 \times 2$  unit cell of BaScO<sub>2</sub>F depicts Ba-F tetrahedral chains, and (b) the structure 0.36 eV/unit cell higher in energy shows Ba-F linear chains. (c) Phonon band structure EuScO<sub>2</sub>F depicting imaginary bands at all special Q points. (d) ModeMap of BaScO<sub>2</sub>F (black) and EuScO<sub>2</sub>F (blue) mapped along A. The ModeMap of BaScO<sub>2</sub>F depicts a harmonic potential and a double anharmonic potential well for EuScO<sub>2</sub>F indicating a propensity for distortion.

constant from 80 to 280 K. Increasing the temperature above 280 K caused a decrease in emission intensity. The emission intensity decreased to 50% of the initial value ( $T_{50}$ ) at 387 K. The thermal stability of emission can also give insight into the quenching behavior of both emissions. To investigate the thermal quenching, the plot of normalized, integrated intensity as a function of temperature can be seen in Figure 4b. The steady decrease in emission intensity with increasing temperature reveals the absence of trap states, indicating that all of the Eu<sup>2+</sup> was substituted onto the Ba<sup>2+</sup> site instead of the Sc<sup>3+</sup> site, which causes defects due to aliovalent substitution. The integrated intensity as a function of temperature can also be fitted to the Arrhenius equation following eq 5 to determine the activation energy ( $E_3$ ).

$$I(T) = \frac{I_0}{1 + Ae^{(-E_a/(kT))}}$$
 (5)

Here, I(T) is the intensity at a given temperature T,  $I_0$  is the initial intensity, A is a constant,  $E_a$  is the activation energy for thermal quenching, and k is Boltzmann's constant. The Arrhenius fit can be seen as the orange line in Figure 4b and yields an activation energy of  $0.32~{\rm eV}$ . This value is larger than other materials such as  ${\rm Ba_3Si_6O_{12}N_2:Eu^{2+}}$  ( $E_a=0.24~{\rm eV}$ ;  $T_{50}>473~{\rm K}$ ) and implies a higher activation energy for thermal quenching. The bandgap of  ${\rm BaScO_2F}$  ( $E_g=3.05~{\rm eV}$ ), however, is smaller than that of  ${\rm Ba_3Si_6O_{12}N_2:Eu^{2+}}$  ( $E_g=3.95~{\rm eV}$ ) and allows thermal quenching via photoionization at increased temperatures to more readily occur. Finally, superimposing all of the emission spectra collected from 80 to 500 K, plotted in Figure S6, reveals that the emission peak retains its overall shape. The two crystal fields around each activator ion show nearly identical optical properties, including similar quenching behavior.

**3.3. DFT Investigation of Local Structure.** The average BaScO<sub>2</sub>F and BaScO<sub>2</sub>F:Eu<sup>2+</sup> synthesized here both undoubtedly adopt the cubic crystal structure based on synchrotron X-ray diffraction. Yet the optical properties of the substituted version lead to a different conclusion. Two emission peaks must stem from two luminescent centers. The source of the

two crystallographic sites must, therefore, stem from local structure distortion induced by  $\mathrm{Eu^{2^+}}$  substitution. The most likely local distortion in a perovskite is a structural distortion due to the size mismatch resulting from the smaller  $\mathrm{Eu^{2^+}}$  substituting for the larger  $\mathrm{Ba^{2^+}}$  potentially causing octahedral tilting. Gener-connected [ $BX_6$ ] octahedra and is the most common perovskite distortion. The distortion arises when the A-site cation is too small for the cubic  $BX_3$  corner-sharing network. Cation displacement or Jahn—Teller distortions of the  $BX_6$  octahedra are also common distortions but are likely not occurring in this system.

DFT calculations have been readily used to model octahedral tilting in perovskite structures that occur as a result of composition or defects. 66 Computational analysis of possible octahedral tilting in the BaScO<sub>2</sub>F:Eu<sup>2+</sup> system first requires the use of supercells to account for the statistical site-sharing between O and F. A 2 × 2 × 2 unit cell of BaScO<sub>2</sub>F with all possible distributions of O and F atoms was enumerated using the "Supercell" software and calculating the static total energy of each optimized structure (Figure S8).37 Examining the anion ordering of the lowest energy structure reveals the formation of Ba-F tetrahedral chains within the crystal structure (Figure 5a). Interestingly, this arrangement of atoms is approximately 0.37 eV/unit cell more favorable than the second lowest energy structure, which contains linear Ba-F chains (Figure 5b). These are ~6 eV lower in energy than the highest energy model. There is a clear energetic preference for the formation of Ba-F tetrahedral chains in the structure versus any other arrangement of fluorine and oxygen atoms in the crystal structure. The structure containing the tetrahedral F chain ordering also contains only one crystallographically independent fluorine site, which is in agreement with the <sup>19</sup>F observation. The presence of M-X chains has been previously reported in oxyfluoride perovskites with TaO<sub>2</sub>F showing a preference for O/F off-axis displacements resulting in M-X chains based on a pair distribution function (PDF) analysis.67

The low energy structural model was then modified by substituting one  $Eu^{2+}$  atom for one  $Ba^{2+}$  atom, corresponding to a 12.5% substitution concentration. Analyzing the fully optimized model (Figure S9) immediately shows a structural distortion. The  $Ba^{2+}$  and  $Sc^{3+}$  atoms have shifted away from their special positions as a result of the  $Eu^{2+}$  substitution. The  $Eu^{2+}$  centered polyhedron is heavily distorted; the polyhedron has a volume of 55.53 Å with a significant bond length distortion index of 0.060 Å and quadratic elongation of 1.05 Å. This distorted environment is caused by octahedral tilting due to the collapse of the cuboctahedral cavity from the substitution of  $Eu^{2+}$  for  $Ba^{2+}$ . The density of states and band structure of this optimized model is provided in Figure S10.

Such a high magnitude of distortion from the substitution of a single atom into the structure was not expected and brings the overall structural stability of this cubic perovskite into question. Thus, the dynamic stability of the host, BaScO<sub>2</sub>F, and the luminescent center, EuScO2F, was analyzed by calculating the phonon band structure. The phonon band structures of BaScO<sub>2</sub>F (Figure S11) and EuScO<sub>2</sub>F (Figure 5c) show the presence of imaginary modes, including at the zoneboundary A (Q = 1/2, 1/2, 1/2), indicating structural instability. Imaginary modes at the zone-boundary have also been identified in a large number of inorganic halide ABX<sub>3</sub> perovskites, which were related to the observation of zone-boundary octahedral tilting. This was confirmed by incrementally tilting the  $[BX_6]$  octahedra and calculating the static total energy of each configuration.<sup>41</sup> The resulting anharmonic double-well potentials signify that zone-boundary octahedral tilting is energetically favorable and is likely to occur in these structures. Similarly, the imaginary bands along the Qpoint path  $\Gamma \rightarrow A$  in BaScO<sub>2</sub>F and EuScO<sub>2</sub>F were probed using ModeMap to calculate the potential for a structural distortion. The ModeMap of BaScO<sub>2</sub>F, shown in Figure 5d as the black curve, depicts a single, harmonic potential well suggesting that the cubic structure is indeed the most energetically favorable. This result is not surprising considering the Rietveld refinement confirms an average cubic structure of BaScO<sub>2</sub>F; thus, the calculated imaginary phonon mode must stem from a different instability.<sup>42</sup> Conversely, the ModeMap of EuScO<sub>2</sub>F (Figure 5d as the blue curve) reveals a double anharmonic potential well, signifying that A zone-boundary octahedral tilting is favorable. The presence of zone-boundary octahedral tilting can be directly related to the tolerance factor. BaScO<sub>2</sub>F has a tolerance factor of 0.997 and does not exhibit tilting. Replacing Ba with Eu causes t to move further away from unity (t = 0.95). This implies that rare-earth inclusion in the perovskite provides a mechanism for distortion.

The octahedral tilting pattern that occurs as a result of the zone-boundary instability is potentially the source of the anomalous dual emission. A  $2 \times 2 \times 4$  supercell of BaScO<sub>2</sub>F was therefore constructed with two Eu<sup>2+</sup> atoms replacing Ba to determine if distortion causes two different coordination environments around the rare earth ion. Structural optimization of this supercell produced a distorted cell containing octahedral tilting that was equivalent to the single substitution site model. Further examination into the tilting reveals in-phase tilting along the a axis and out-of-phase tilting along the b and c axes (Figure 6a). Because the magnitudes of octahedral tilting along b and c are different, the Glazer notation for the observed octahedral tilting in this perovskite is  $a^+b^-c^{-.68}$  This tilt system uniquely belongs to the  $P2_1/m$  space group. This is a critical outcome because that means the local symmetry of this

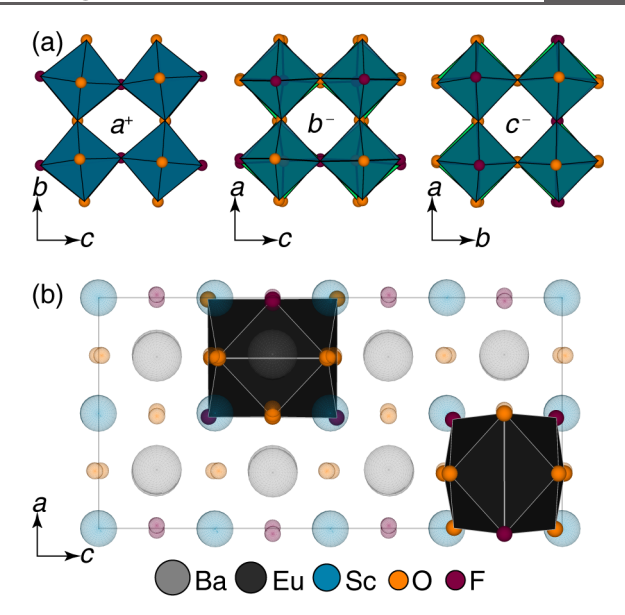


**Figure 6.** (a) Octahedral tilting along the *a, b,* and *c* axes exhibiting the overall  $a^+b^-c^-$  Glazer tilt system. Only one unit cell from the overall  $2 \times 2 \times 4$  supercell is shown for clarity. (b) Drawing the polyhedra around the Eu clearly shows two different polyhedral environments.

perovskite can be described as  $P2_1/m$ , even though the average symmetry of  $Ba_{0.96}Eu_{0.04}ScO_2F$  appears cubic. This is further surprising because analyzing the average tolerance factor for the compound would not have suggested a potential structure distortion. Calculating the modified Goldschmidt tolerance factor to accommodate for the substitution of  $Eu^{2+}$  on the 12-coordinate  $Ba^{2+}$  site in  $ABO_2F$  structure type using eq 6, where  $r_A$ ,  $r_B$ ,  $r_{RE}$ ,  $r_O$ ,  $r_F$  are the ionic radii of A, B, the rare-earth atom, O, and F ions, respectively, and x is the amount of  $Eu^{2+}$  substitution, shows only adding 4%  $Eu^{2+}$  (the concentration measured using synchrotron scattering) causes the tolerance factor to only minimally decrease to a value of 0.995. Thus,  $Ba_{0.96}Eu_{0.04}ScO_2F$  would also be incorrectly predicted to have an overall average cubic structure.

$$t = \frac{(1 - x)r_A + (x)r_{RE} + 0.66r_O + 0.33r_F}{\sqrt{2}(r_B + 0.66r_O + 0.33r_F)}$$
(6)

However, the synthesized compound is composed of a majority of BaScO<sub>2</sub>F units, which are not predicted to tilt, but the structure also contains locally coordinated EuScO<sub>2</sub>F unit cells that are expected to tilt. The presence of the distorted unit cells acts as point defects that propagate across the compound and induces a distortion that influences the entire crystal structure. Cubic symmetry is still observed, however, because the average structure does not distort sufficiently to cause the expected 131, 113, and 311 reflections. 65 Techniques that retain the local structure, like PDF, should resolve this structural conundrum. Indeed, a PDF analysis of the isostructural BaInO<sub>2</sub>F revealed that the tilting of the BX<sub>6</sub> octahedra caused the local symmetry to lower from cubic to triclinic. The the short-range (<10 Å) PDF data describing the local structure could only be fit according to triclinic symmetry, whereas the long-range (>10 Å) PDF data describing the average structure could be reliably fit to a cubic model.<sup>27</sup> A similar investigation could be done for Ba<sub>0.98</sub>Eu<sub>0.002</sub>ScO<sub>2</sub>F, although the distortion may be too subtle to be resolved even through PDF analysis.

More importantly, the loss of local symmetry from  $Pm\overline{3}m$  to P2<sub>1</sub>/m results in two crystallographically independent A cations (A and A').65 This allows for the formation of rareearth environments with different the polyhedral geometries. Analyzing the DFT optimized local structure around Eu(1)and Eu(2) shows they slightly differ; Eu(1) has a polyhedral volume of 59.41 Å<sup>3</sup>, whereas Eu(2) has a larger polyhedral volume of 59.60 Å<sup>3</sup> (Figure 6b). The minor differences in bond length and geometry for each Eu<sup>2+</sup> coordination environment are sufficient to induce changes in the crystal field splitting of the Eu 5d orbitals, the centroid shift, and the Stokes' shift. 70,71 Considering the observed emission peaks are primarly dictated by subtle changes in the crystal field splitting, it is important to calculate these effects, which can be done through eq 7.19 Crystal field splitting is dependent upon the bond length, degree of covalency between activator ion to coordinating ion, the coordination environment, and the symmetry of the substitution site.<sup>63</sup> The degree of covalency and the coordination environment will not affect the crystal field splitting because these parameters are identical for both Eu2+ atoms. Therefore, crystal field splitting can be approximated by directly relating bond length, as dictated by the symmetry, to the energy level substitution.

$$D_{q} = \frac{Ze^{2}r^{4}}{6R^{5}} \tag{7}$$

Using eq 7 and the calculated bond lengths from firstprinciples calculation (Table S3) shows that the crystal field splitting between the two Eu<sup>2+</sup> ions in this model differs by  $\approx$ 1%. This difference, although small, is still sufficient to give rise to the anomalies in the luminescent data, where the presence of the second emission is only visible as an asymmetric emission at longer wavelengths. The small difference also supports the difficulty in resolving these two peaks, even at ~10 K. These results express a need to be cautious in exploring perovskites as a route to narrow-emitting phosphors. The size mismatch between the rare-earth and Asite cation should be minimized to prevent large magnitudes of octahedral tilting, and the resulting Glazer tilt system should be investigated to determine the number of crystallographically independent cation sites. Crystal structures prone to distortion, such as perovskites, should be extensively studied using highresolution crystallography and first-principles calculations together to confirm that the host is viable to produce highly efficient and narrow emission.

#### 4. CONCLUSIONS

In the quest to produce a phosphor with highly efficient, narrow emission, a new cyan-emitting phosphor BaScO<sub>2</sub>F:Eu<sup>2+</sup> perovskite has been identified. Luminescent data revealed a surprising broad emission with a full width at half-maximum of 4135 cm<sup>-1</sup> (103 nm). Room temperature and temperature-dependent lifetime measurements corroborated the presence of two emission peaks rather than the single peak that was expected. The phonon band structure reveals imaginary modes consistent with an inherent instability of the local EuScO<sub>2</sub>F luminescent center. The local structure is prone to distortion, producing the  $a^+b^-c^-$  octahedral tilting pattern and induces a subtle but global distortion that gives rise to two independent substitution sites. As a result, the magnitudes of crystal field splitting for the two Eu<sup>2+</sup> sites differ, producing distinct optical properties that could not have been correctly interpreted

without the aid of computational analysis. These results not only suggest that perovskites may not be suitable hosts for narrow emission in phosphors despite their high symmetry but also provide broader implications to the perovskite community. Compounds and crystal structures on the verge of instabilities need to be exhaustively probed to understand the structure—composition—property relationship.

# ASSOCIATED CONTENT

# **Supporting Information**

The Supporting Information is available free of charge at https://pubs.acs.org/doi/10.1021/acs.chemmater.0c02062.

X-ray powder patterns, Le Bail and Rietveld refinement results, temperature-dependent emission specta, and computational results of total static energy calculations, structure optimizations, and electronic structure calculations (PDF)

#### AUTHOR INFORMATION

### **Corresponding Author**

Jakoah Brgoch — Department of Chemistry, University of Houston, Houston, Texas 77204, United States; orcid.org/0000-0002-1406-1352; Email: jbrgoch@uh.edu

#### Author

Shruti Hariyani — Department of Chemistry, University of Houston, Houston, Texas 77204, United States; orcid.org/0000-0002-4707-8863

Complete contact information is available at: https://pubs.acs.org/10.1021/acs.chemmater.0c02062

#### Notes

The authors declare no competing financial interest.

# ACKNOWLEDGMENTS

The authors thank Professor Jiming Bao and Guang Yang for conducting the 10 K luminescent measurements. The authors also thank the National Science Foundation (Grant CER 19-11311) as well as the Welch Foundation (Grant E-1981) for supporting this work. This research used the Maxwell/Opuntia/Sabine cluster(s) operated by the Research Computing Data Core at the University of Houston. This work used the resources available through the 11-BM beamline at the Advanced Photon Source, an Office of Science User Facility operated for the U.S. Department of Energy (DOE) Office of Science by Argonne National Laboratory, under Contract DE-AC02-06CH11357.

#### REFERENCES

- (1) Schubert, E. F.; Kim, J. K. Solid-state light sources getting smart. *Science* **2005**, *308* (5726), 1274–1278.
- (2) Strobel, P.; Maak, C.; Weiler, V.; Schmidt, P. J.; Schnick, W. Ultra-narrow-band blue-emitting oxoberyllates AELi<sub>2</sub>[Be<sub>4</sub>O<sub>6</sub>]:Eu<sup>2+</sup> (AE=Sr,Ba) Paving the Way to Efficient RGB pc-LEDs. Angew. Chem., Int. Ed. 2018, 57 (28), 8739–8743.
- (3) Qin, X.; Liu, X.; Huang, W.; Bettinelli, M.; Liu, X. Lanthanide-Activated Phosphors Based on 4f-5d Optical Transitions: Theoretical and Experimental Aspects. *Chem. Rev.* **2017**, *117* (5), 4488–4527.
- (4) Pust, P.; Schmidt, P. J.; Schnick, W. A revolution in lighting. *Nat. Mater.* **2015**, *14* (5), 454–458.
- (5) Lustig, W. P.; Shen, Z.; Teat, S. J.; Javed, N.; Velasco, E.; O'Carroll, D. M.; Li, J. Rational design of a high-efficiency,

- multivariate metal—organic framework phosphor for white LED bulbs. Chem. Sci. 2020, 11 (7), 1814–1824.
- (6) Zhu, H.; Lin, C. C.; Luo, W.; Shu, S.; Liu, Z.; Liu, Y.; Kong, J.; Ma, E.; Cao, Y.; Liu, R.-S.; Chen, X. Highly efficient non-rare-earth red emitting phosphor for warm white light-emitting diodes. *Nat. Commun.* **2014**, *5* (1), 4312.
- (7) Jüstel, T.; Nikol, H.; Ronda, C. New developments in the field of luminescent materials for lighting and displays. *Angew. Chem., Int. Ed.* **1998**, *37* (22), 3084–3103.
- (8) Xie, R.-J.; Hirosaki, N.; Takeda, T. Wide color gamut backlight for liquid crystal displays using three-band phosphor-converted white light-emitting diodes. *Appl. Phys. Express* **2009**, *2*, No. 022401.
- (9) Phillips, J. M.; Coltrin, M. E.; Crawford, M. H.; Fischer, A. J.; Krames, M. R.; Mueller-Mach, R.; Mueller, G. O.; Ohno, Y.; Rohwer, L. E. S.; Simmons, J. A.; Tsao, J. Y. Research challenges to ultra-efficient inorganic solid-state lighting. *Laser Photonics Rev.* **2007**, *1* (4), 307–333.
- (10) Liao, H.; Zhao, M.; Molokeev, M. S.; Liu, Q.; Xia, Z. Learning from a mineral structure toward an ultra-narrow-band blue-emitting silicate phosphor RbNa<sub>3</sub>(Li<sub>3</sub>SiO<sub>4</sub>)<sub>4</sub>:Eu<sup>2+</sup>. *Angew. Chem., Int. Ed.* **2018**, 57 (36), 11728–11731.
- (11) Strobel, P.; de Boer, T.; Weiler, V.; Schmidt, P. J.; Moewes, A.; Schnick, W. Luminescence of an oxonitridoberyllate: A study of narrow-band cyan-emitting Sr[Be<sub>6</sub>ON<sub>4</sub>]:Eu<sup>2+</sup>. *Chem. Mater.* **2018**, *30* (9), 3122–3130.
- (12) Kim, K.-B.; Kim, Y.-I.; Chun, H.-G.; Cho, T.-Y.; Jung, J.-S.; Kang, J.-G. Structural and optical properties of BaMgAl<sub>10</sub>O<sub>17</sub>:Eu<sup>2+</sup> phosphor. *Chem. Mater.* **2002**, *14* (12), 5045–5052.
- (13) Takeda, T.; Hirosaki, N.; Funahshi, S.; Xie, R.-J. Narrow-band green-emitting phosphor Ba<sub>2</sub>LiSi<sub>7</sub>AlN<sub>12</sub>:Eu<sup>2+</sup> with high thermal stability discovered by a single particle diagnosis approach. *Chem. Mater.* **2015**, 27 (17), 5892–5898.
- (14) Pust, P.; Weiler, V.; Hecht, C.; Tücks, A.; Wochnik, A. S.; Henß, A.-K.; Wiechert, D.; Scheu, C.; Schmidt, P. J.; Schnick, W. Narrow-band red-emitting Sr[LiAl<sub>3</sub>N<sub>4</sub>]:Eu<sup>2+</sup> as a next-generation LED-phosphor material. *Nat. Mater.* **2014**, *13*, 891–896.
- (15) Duke, A. C.; Hariyani, S.; Brgoch, J. Ba<sub>3</sub>Y<sub>2</sub>B<sub>6</sub>O<sub>15</sub>:Ce<sup>3+</sup>—A high symmetry, narrow-emitting blue phosphor for wide-gamut white lighting. *Chem. Mater.* **2018**, 30 (8), 2668–2675.
- (16) Akella, A.; Keszler, D. A. Structure and Eu<sup>2+</sup> luminescence of dibarium magnesium orthoborate. *Mater. Res. Bull.* **1995**, 30 (1), 105–111.
- (17) Zhuo, Y.; Mansouri Tehrani, A.; Oliynyk, A. O.; Duke, A. C.; Brgoch, J. Identifying an efficient, thermally robust inorganic phosphor host via machine learning. *Nat. Commun.* **2018**, *9* (1), 4377.
- (18) Maekawa, T.; Kurosaki, K.; Yamanaka, S. Thermal and mechanical properties of perovskite-type barium hafnate. *J. Alloys Compd.* **2006**, *407* (1), 44–48.
- (19) George, N. C.; Denault, K. A.; Seshadri, R. Phosphors for solid-state white lighting. *Annu. Rev. Mater. Res.* **2013**, 43 (1), 481–501.
- (20) Dorenbos, P. Anomalous luminescence of Eu<sup>2+</sup> and Yb<sup>2+</sup> in inorganic compounds. *J. Phys.: Condens. Matter* **2003**, *15* (17), 2645–2665.
- (21) Katyayan, S.; Agrawal, S. Molten salt synthesis and photoluminescent studies of  $ATiO_3$ :Eu<sup>2+</sup>, Yb<sup>2+</sup> (A = Ca, Ba, Sr) perovskites phosphors. *J. Photonics Energy* **2018**, 8 (3), 036001.
- (22) Majher, J. D.; Gray, M. B.; Strom, T. A.; Woodward, P. M. Cs<sub>2</sub>NaBiCl<sub>6</sub>:Mn<sup>2+</sup>—A new orange-red halide double perovskite phosphor. *Chem. Mater.* **2019**, *31* (5), 1738–1744.
- (23) Sharits, A. R.; Khoury, J. F.; Woodward, P. M. Evaluating  $NaREMgWO_6$  (RE = La, Gd, Y) Doubly Ordered Double Perovskites as  $Eu^{3+}$  Phosphor Hosts. *Inorg. Chem.* **2016**, 55 (23), 12383–12390.
- (24) Smith, M. D.; Jaffe, A.; Dohner, E. R.; Lindenberg, A. M.; Karunadasa, H. I. Structural origins of broadband emission from layered Pb–Br hybrid perovskites. *Chem. Sci.* **2017**, 8 (6), 4497–4504.
- (25) Tan, Z.; Li, J.; Zhang, C.; Li, Z.; Hu, Q.; Xiao, Z.; Kamiya, T.; Hosono, H.; Niu, G.; Lifshitz, E.; Cheng, Y.; Tang, J. Highly efficient blue-emitting Bi-doped Cs<sub>2</sub>SnCl<sub>6</sub> perovskite variant: Photolumines-

- cence induced by impurity doping. Adv. Funct. Mater. 2018, 28 (29), 1801131.
- (26) Heap, R.; Slater, P. R.; Berry, F. J.; Helgason, O.; Wright, A. J. Synthesis and structural determination of the new oxide fluoride BaFeO<sub>2</sub>F. *Solid State Commun.* **2007**, *141* (8), 467–470.
- (27) Katsumata, T.; Suzuki, R.; Satoh, N.; Suzuki, S.; Nakashima, M.; Inaguma, Y.; Mori, D.; Aimi, A.; Yoneda, Y. Synthesis of new perovskite-type oxyfluorides, BaInO<sub>2</sub>F and comparison of the structure among perovskite-type oxyfluorides. *J. Solid State Chem.* **2019**, 279, 120919.
- (28) Needs, R. L.; Weller, M. T. A New  $2^+/3^+$  Perovskite: The Synthesis and Structure of BaScO<sub>2</sub>F. *J. Solid State Chem.* **1998**, 139 (2), 422–423.
- (29) Toby, B. H.; EXPGUI, H. a graphical user interface for GSAS. *J. Appl. Crystallogr.* **2001**, 34 (2), 210–213.
- (30) Momma, K.; Izumi, F. VESTA 3 for three-dimensional visualization of crystal, volumetric, and morphology data. *J. Appl. Crystallogr.* **2011**, *44*, 1272–1276.
- (31) de Mello, J. C.; Wittmann, H. F.; Friend, R. H. An improved experimental determination of external photoluminescence quantum efficiency. *Adv. Mater.* **1997**, *9* (3), 230–232.
- (32) Kresse, G.; Furthmüller, J. Efficient iterative schemes for ab initio total-energy calculations using a plane-wave basis set. *Phys. Rev. B: Condens. Matter Mater. Phys.* **1996**, 54 (16), 11169–11186.
- (33) Blöchl, P. E. Projector augmented-wave method. *Phys. Rev. B: Condens. Matter Mater. Phys.* **1994**, *50* (24), 17953–17979.
- (34) Perdew, J. Density functional theory and the band gap problem. *Int. J. Quantum Chem.* **1985**, 28 (S19), 497–523.
- (35) Francisco, E.; Recio, J. M.; Blanco, M. A.; Pendás, A. M.; Costales, A. Quantum-mechanical study of thermodynamic and bonding properties of MgF<sub>2</sub>. *J. Phys. Chem. A* **1998**, *102* (9), 1595–1601.
- (36) Wu, Z. -j.; Zhao, E. -j.; Xiang, H. -p.; Hao, X. -f.; Liu, X. -j.; Meng, J. Crystal structures and elastic properties of superhard IrN<sub>2</sub> and IrN<sub>3</sub> from first principles. *Phys. Rev. B: Condens. Matter Mater. Phys.* **2007**, 76 (5), No. 054115.
- (37) Okhotnikov, K.; Charpentier, T.; Cadars, S. Supercell program: a combinatorial structure-generation approach for the local-level modeling of atomic substitutions and partial occupancies in crystals. *J. Cheminf.* **2016**, 8 (1), 17.
- (38) Monkhorst, H. J.; Pack, J. D. Special points for Brillouin-zone integrations. *Phys. Rev. B: Condens. Matter Mater. Phys.* **1976**, 13 (12), 5188–5192.
- (39) Finley, E.; Mansouri Tehrani, A.; Brgoch, J. Intrinsic defects drive persistent luminescence in monoclinic SrAl<sub>2</sub>O<sub>4</sub>:Eu<sup>2+</sup>. *J. Phys. Chem. C* **2018**, *122* (28), 16309–16314.
- (40) Parlinski, K.; Li, Z. Q.; Kawazoe, Y. First-principles determination of the soft mode in cubic ZrO<sub>2</sub>. *Phys. Rev. Lett.* **1997**, 78 (21), 4063–4066.
- (41) Skelton, J. M.; Burton, L. A.; Parker, S. C.; Walsh, A.; Kim, C.-E.; Soon, A.; Buckeridge, J.; Sokol, A. A.; Catlow, C. R. A.; Togo, A.; Tanaka, I. Anharmonicity in the high-temperature *Cmcm* phase of SnSe: Soft modes and three-phonon interactions. *Phys. Rev. Lett.* **2016**, *117* (7), No. 075502.
- (42) Yang, R. X.; Skelton, J. M.; da Silva, E. L.; Frost, J. M.; Walsh, A. Assessment of dynamic structural instabilities across 24 cubic inorganic halide perovskites. *J. Chem. Phys.* **2020**, *152* (2), No. 024703.
- (43) Chin, X. Y.; Cortecchia, D.; Yin, J.; Bruno, A.; Soci, C. Lead iodide perovskite light-emitting field-effect transistor. *Nat. Commun.* **2015**, *6* (1), 7383.
- (44) Lizzo, S.; Klein, E. P.; Nagelvoort, N.; Erens, R.; Meijerink, A.; Blasse, G. On the quenching of the Yb<sup>2+</sup> lumienscence in different host lattices. *J. Phys. Chem. Solids* **1997**, *58* (6), 963–968.
- (45) Khamari, B.; Nanda, B. R. K. Shifting of Fermi level and realization of topological insulating phase in the oxyfluoride BaBiO<sub>2</sub>F. *Mater. Res. Express* **2019**, *6* (6), No. 066309.

- (46) Chen, D.; Wang, Y.; Yu, Y.; Ma, E.; Zhou, L. Microstructure and luminescence of transparent glass ceramic containing Er<sup>3+</sup>:BaF<sub>2</sub> nano-crystals. *J. Solid State Chem.* **2006**, *179* (2), 532–537.
- (47) Denault, K. A.; George, N. C.; Paden, S. R.; Brinkley, S.; Mikhailovsky, A. A.; Neuefeind, J.; DenBaars, S. P.; Seshadri, R. A green-yellow emitting oxyfluoride solid solution phosphor  $Sr_2Ba-(AlO_4F)_{1-x}(SiO_5)_x:Ce^{3+}$  for thermally stable, high color rendition solid state white lighting. *J. Mater. Chem.* **2012**, 22 (35), 18204–18213
- (48) Im, W. B.; Brinkley, S.; Hu, J.; Mikhailovsky, A.; DenBaars, S. P.; Seshadri, R. Sr<sub>2.975-x</sub>Ba<sub>x</sub>Ce<sub>0.025</sub>AlO<sub>4</sub>F: a highly efficient greenemitting oxyfluoride phosphor for solid state white lighting. *Chem. Mater.* **2010**, 22 (9), 2842–2849.
- (49) Zen, E.-a. Validity of "Vegard's law". Am. Mineral. 1956, 41 (5-6), 523-524.
- (50) Schoop, L. M.; Müchler, L.; Felser, C.; Cava, R. J. Lone pair effect, structural distortions, and potential for superconductivity in Tl perovskites. *Inorg. Chem.* **2013**, 52 (9), 5479–5483.
- (51) Stewart, R. F. Generalized X-Ray scattering factors. J. Chem. Phys. **1969**, 51 (10), 4569-4577.
- (52) Shannon, R. D.; Prewitt, C. T. Effective ionic radii in oxides and fluorides. *Acta Crystallogr., Sect. B: Struct. Crystallogr. Cryst. Chem.* **1969**, 25 (5), 925–946.
- (53) Zhou, W.; Han, J.; Zhang, X.; Qiu, Z.; Xie, Q.; Liang, H.; Lian, S.; Wang, J. Synthesis and photoluminescence properties of a cyanemitting phosphor  $Ca_3(PO_4)_2$ :Eu<sup>2+</sup> for white light-emitting diodes. *Opt. Mater.* **2015**, *39*, 173–177.
- (54) Zhong, J.; Zhuo, Y.; Hariyani, S.; Zhao, W.; Wen, J.; Brgoch, J. Closing the cyan gap toward full-spectrum LED lighting with NaMgBO<sub>3</sub>:Ce<sup>3+</sup>. Chem. Mater. **2020**, 32 (2), 882–888.
- (55) Fang, M.-H.; Ni, C.; Zhang, X.; Tsai, Y.-T.; Mahlik, S.; Lazarowska, A.; Grinberg, M.; Sheu, H.-S.; Lee, J.-F.; Cheng, B.-M.; Liu, R.-S. Enhance color rendering index via full spectrum employing the important key of cyan phosphor. *ACS Appl. Mater. Interfaces* **2016**, 8 (45), 30677–30682.
- (56) Blasse, G. Energy transfer between inequivalent Eu<sup>2+</sup> ions. *J. Solid State Chem.* **1986**, 62 (2), 207–211.
- (57) Poort, S. H. M.; Reijnhoudt, H. M.; van der Kuip, H. O. T.; Blasse, G. Luminescence of Eu<sup>2+</sup> in silicate host lattices with alkaline earth ions in a row. *J. Alloys Compd.* **1996**, *241* (1), 75–81.
- (58) Poort, S. H. M.; Meyerink, A.; Blasse, G. Lifetime measurements in Eu<sup>2+</sup>-doped host lattices. *J. Phys. Chem. Solids* **1997**, *58* (9), 1451–1456
- (59) Xiao, W.; Zhang, X.; Hao, Z.; Pan, G.-H.; Luo, Y.; Zhang, L.; Zhang, J. Blue-emitting  $K_2Al_2B_2O_7$ :  $Eu^{2+}$  phosphor with high thermal stability and high color purity for near-UV-pumped white lightenitting diodes. *Inorg. Chem.* **2015**, *54* (7), 3189–3195.
- (60) Hariyani, S.; Armijo, E.; Brgoch, J. Broad green emission in the leucite-like Cs<sub>2</sub>ZnSi<sub>5</sub>O<sub>12</sub>:Eu<sup>2+</sup> phosphor. ECS J. Solid State Sci. Technol. **2020**, 9 (1), No. 016015.
- (61) Chen, G.; Zhuang, W.; Hu, Y.; Liu, Y.; Liu, R.; He, H. Luminescence properties of Eu<sup>2+</sup>-doped Ba<sub>3</sub>Si<sub>6</sub>O<sub>12</sub>N<sub>2</sub> green phosphor: concentration quenching and thermal stability. *J. Rare Earths* **2013**, *31* (2), 113–118.
- (62) Tang, J.; Chen, J.; Hao, L.; Xu, X.; Xie, W.; Li, Q. Green  $Eu^{2+}$ doped  $Ba_3Si_6O_{12}N_2$  phosphor for white light-emitting diodes: Synthesis, characterization and theoretical simulation. *J. Lumin.* **2011**, *131* (6), 1101–1106.
- (63) Rack, P. D.; Holloway, P. H. The structure, device physics, and material properties of thin film electroluminescent displays. *Mater. Sci. Eng., R* **1998**, *21* (4), 171–219.
- (64) Bechtel, J. S.; Van der Ven, A. Octahedral tilting instabilities in inorganic halide perovskites. *Phys. Rev. Mater.* **2018**, 2 (2), No. 025401.
- (65) Woodward, P. M. Octahedral Tilting in Perovskites. I. Geometrical Considerations. *Acta Crystallogr., Sect. B: Struct. Sci.* **1997**, *B*53, 32–43.
- (66) Maughan, A. E.; Ganose, A. M.; Almaker, M. A.; Scanlon, D. O.; Neilson, J. R. Tolerance Factor and Cooperative Tilting Effects in

- Vacancy-Ordered Double Perovskite Halides. Chem. Mater. 2018, 30 (11), 3909–3919.
- (67) Ngaruiya, J. M.; Nieuwoudt, S.; Ntwaeaborwa, O. M.; Terblans, J. J.; Swart, H. C. Resolution of Eu2+ asymmetrical emission peak of SrAl2O4:Eu2+, Dy3+ phosphor by cathodoluminescence measurements. *Mater. Lett.* **2008**, *62* (17), 3192–3194.
- (68) Glazer, A. M. Simple ways of determining perovskite structures. *Acta Crystallogr., Sect. A: Cryst. Phys., Diffr., Theor. Gen. Crystallogr.* 1975, 31 (6), 756–762.
- (69) Sato, T.; Takagi, S.; Deledda, S.; Hauback, B. C.; Orimo, S.-i. Extending the applicability of the Goldschmidt tolerance factor to arbitrary ionic compounds. *Sci. Rep.* **2016**, *6* (1), 23592.
- (70) Qiao, J.; Zhou, G.; Zhou, Y.; Zhang, Q.; Xia, Z. Divalent europium-doped near-infrared-emitting phosphor for light-emitting diodes. *Nat. Commun.* **2019**, *10* (1), 5267.
- (71) Zhao, M.; Xia, Z.; Huang, X.; Ning, L.; Gautier, R.; Molokeev, M. S.; Zhou, Y.; Chuang, Y.-C.; Zhang, Q.; Liu, Q.; Poeppelmeier, K. R. Li substituent tuning of LED phosphors with enhanced efficiency, tunable photoluminescence, and improved thermal stability. *Science Advances* **2019**, *5* (1), eaav0363.